Check for updates

Advanced Sensor Research

ADVANCED SENSOR RESEARCH Open Access

www.advsensorres.com

RESEARCH ARTICLE OPEN ACCESS

Toward Intelligent Adhesive Fibrillary Gripping Systems: Soft Coil–Based Misalignment And Shape Sensing

Simon Herter[1,2] | Sarah C.L. Fischer[1]

[1]Fraunhofer Institute for Nondestructive Testing IZFP, Saarbruecken, Germany | [2]Department of Systems Engineering, Saarland University, Saarbruecken, Germany

Correspondence: Simon Herter (simon.herter@izfp.fraunhofer.de)

Received: 23 January 2026 | **Revised:** 8 June 2026 | **Accepted:** 11 June 2026

Keywords: coil sensing | machine learning | misalignment detection | real-time monitoring | shape estimation | soft sensor

ABSTRACT

Bioinspired microstructured gripping systems for robots are promising solutions for future pick-and-place applications in industrial plants thanks to their energy self-sufficiency. However, the absence of a control variable limits auto-adaptive automation. To overcome this limitation, we present a coil-based soft sensor capable of detecting angular misalignment during continuous motion, as well as object shape discrimination between planar and convex shaped objects. The sensing concept is first demonstrated on activated adhesive structures, demonstrating a transition from laboratory to application. The system's angular detection performance is evaluated across a test matrix covering step-by-step and continuous robot operation, multiple velocity levels (e.g. 2 mms^{-1}, 5 mms^{-1}, and 10 mms^{-1}), and both TRF and WRF. Across all tested configurations, a maximum RMSE of 0.21 ° is achieved. For object shape classification, a kNN classifier is trained and validated using a leave-one-group-out cross-validation, where each group corresponds to one measurement series of a single object class. Accuracy for different groups range from 97 % to 100 %. After applying majority voting with a 99 % confidence threshold 494 out of 495 measurements are correctly classified. Future work will extend the sensor evaluation by incorporating additional parameters such as contact area and pressure.

1 | Introduction

Robots equipped with soft end effectors as well as fully soft robotic systems have emerged as a rapidly developing technology that has gained significant attention in recent research. Due to their flexibility and compliance, these systems overcome the inherent limitations of traditional rigid handling mechanisms, enabling novel applications. However, the high degree of freedom poses challenges in terms of gripper control, which makes integrated sensor technology necessary [1–5].

Specifically bioinspired microstructured adhesive surfaces offer the advantage of operating without external energy input while still being able to manipulate relatively large loads [6–9]. Since the adhesive force of these bioinspired adhesive structures depends on the alignment of the structures to the objects, a control and feedback loop is necessary to perform a reliable handling process. Even small angular deviations of less than 1 ° are important for the generated adhesive force [10]. For this reason, tactile sensors for measuring tilt and alignment are desirable for bioinspired adhesive pads [11, 12].

To solve the control and feedback problem, concepts of tactile sensors based on a wide variety of physical interactions have been developed, including magnetic [13–15], optic [16–22] and electromagnetic (eddy current, resistive) [23–28] sensors for measuring misalignment and control parameters.

Current research in tactile sensing uses magnetic field-based approaches, as exemplified by e-Flesh [15], AnySkin [14], and ReSkin [13], which offer low-cost, scalable, and fabrication-friendly solutions for embedding dense tactile sensing into

This is an open access article under the terms of the Creative Commons Attribution License, which permits use, distribution and reproduction in any medium, provided the original work is properly cited.

© 2026 The Author(s). *Advanced Sensor Research* published by Wiley-VCH GmbH

robotic systems. These sensors typically rely on compliant structures that transduce surface deformation into variations in magnetic fields, enabling the estimation of contact location and force through data-driven methods. However, the design and material composition required to house magnetic elements and deformable layers would influence the overall stiffness of bioinspired gripping systems. In parallel optical sensors are becoming more and more popular for tactile perception in robotics. Systems such as GelSight [16], GelSim [17], GelSim-3 [20] and GelSim-4 [22], estimate contact states and surface characteristics by visually tracking deformations of compliant interfaces. Such vision based systems like Viko [18] and Viko 2.0 [19] have already been tested on wedge shaped gecko-inspired adhesive in robotic gripping. In the field of electromagnetic sensor technology, reconfigurable sensors have been developed for force and torque measurement in robotics. These sensors provide precise and reliable predictions and are also cost-effective [25]. In our previous research [24], we were able to show that our coil-based sensor technology is suitable for implementation as tactile sensor technology in bioinspired gripping systems with precise angle predictions. However, sensor technology was limited to work on planar surfaces because of the three receiving coils, thus, not enabling the application for spherical and curved objects.

In the present work, we build on these findings by adding a fourth coil to our tactile sensor, which increases the resolution of the system and, thus, circumvents the limitations of the previous system. Enabling improved generalization across a wider range of object shapes. In addition, this study moves from laboratory to industrial standard by testing activated adhesive structures. The entire sensor design is geared toward flexibility, speed, and scalability in order to meet the requirements of industry as closely as possible.

In this study we extend our previous tactile sensor platform by integrating a fourth excitation coil, thereby raising spatial resolution and eliminating the sampling constraints that limited earlier prototypes. The higher density coil array enables robust generalization across a broader spectrum of object geometries, improving shape discrimination performance. The device is advanced from a laboratory proof-of-concept to an industrial-grade system by assessing its performance with commercially relevant activated adhesive structures. The sensor architecture is intentionally engineered for mechanical flexibility, fast response, and straightforward scalability, thereby satisfying the practical requirements of manufacturing environments.

2 | Experimental Section

2.1 | Sensor Stack

The sensor stack is designed as a modular concept, see Figure 1a. Consisting of the following four components:

1. Sensing layer (PCB-based sensor coils)
2. Deformable layer
3. Measuring layer
4. Adhesive bioinspired pad

The novel sensor system (PCB coils) is integrated into the commercially available adhesive gripper from Innocise GmbH. The adhesive gripper consists of a microstructured adhesive pad (Innocise GmbH) and a foam layer (KS 865 F Klebeshop 24), which makes the stack adaptable. To measure the deformation of the adhesive structure, a conductive fabric (Shieldex Kassel Statex Produktions- und Vertriebs GmbH) is inserted between the foam and the adhesive pad.

The printed circuit board (PCB) layout comprises a transmitter coil with three layers and a diameter of 24 mm, complemented by four receiver coils, each measuring approximately 6 mm in diameter. Furthermore, provisions for the integration of passive electrical components were incorporated into the layout, although these elements are not central to the present investigation. Finally, the design is completed by the integration of spring contacts, which are mounted directly onto the PCB. This feature enables modular configuration, facilitates replacement of the sensor system and allows implementation as a quick-change system. For experiments, the sensor stack is mounted on the robot Figure 1b using the quick-change system, see Figure 1c. This study employs adhesive pads with modified tip geometry, so-called mushroom tips, specifically engineered to maximize the adhesive force. This design ensures that the experimental setup closely mirrors conditions relevant to industrial applications, thus enhancing the practical significance of the results.

2.2 | Measuring Setup

The measurement setup consists of a Meca 500R3 6-axis robot (Mecademic) for manipulating the sensor stack in space. A 3-axis force sensor (K3D100 ME-Meßsysteme GmbH) with a value range of ± 100 N is attached to its flange, to which the developed sensor stack is connected. In addition, the setup features an optical reference setup based on the frustrated total internal reflection (FTIR) principle, for which a setup including a glass plate, LED lighting and a mirror with a camera (DFK 23UP031 equipped with TPL 0820 7MP lens from The Imaging Source Europe GmbH) is installed in front of the robot. Furthermore, an Arduino with environmental sensors for light (TSL2591) as well as temperature, humidity and pressure (GYBMEP) is placed in the robot cell to track environmental conditions during all experiments. Due to the planar glass plate, this setup can be used for all misalignment measurements. For measurements on convex surfaces, a test body containing four convex shapes was designed using a 3D printing process. These shapes have a diameter of 56 mm each and radii of 40 mm, 60 mm, 80 mm and 100 mm, respectively.

2.3 | Alignment and Calibration

Calibration is an essential part of the evaluation process in order to be able to evaluate the sensor data. However, a suitable reference must be established before the calibration curves are recorded. Since there is no perfect alignment due to tolerances in the system and adhesive pads, an alignment is performed using

27511219, 2026, 7, Downloaded from https://advanced.onlinelibrary.wiley.com/doi/10.1002/adsr.70172 by Birgit Conrad-Markschläger - Fraunhofer IZFP , Wiley Online Library on [07/07/2026]. See the Terms and Conditions (https://onlinelibrary.wiley.com/terms-and-conditions) on Wiley Online Library for rules of use; OA articles are governed by the applicable Creative Commons License

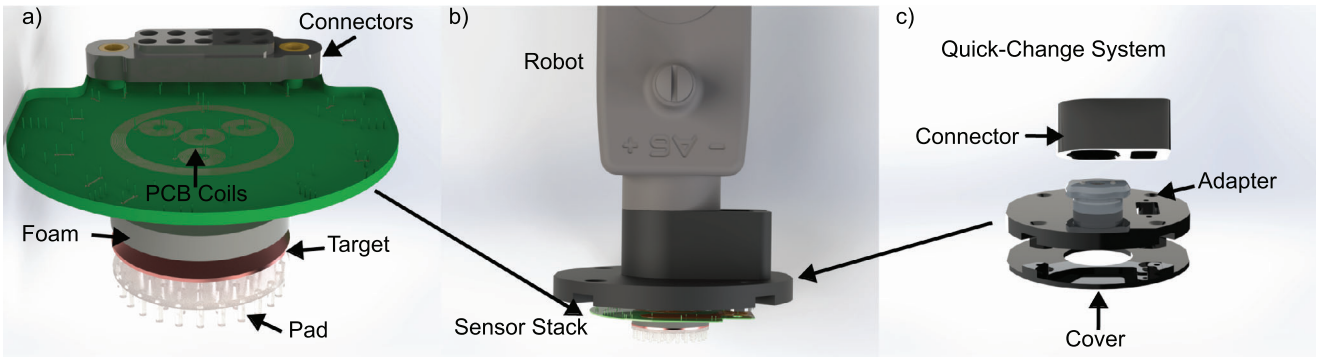

FIGURE 1 | Schematic of sensor stack and quick-change system: (a) Sensor stack with PCB coils and pin ball connectors, to the PCB the deformable foam layer as well as the conductive foam layer is attached, followed by the adhesive pad. (b) Assembly of sensor stack with the quick-change system mounted on a Meca 500R3 Robot. (c) Overview of the quick-change system with the adapter, housing the sensor stack and the modular connector to the robot as well as the cover.

the optical FTIR setup, which allows for the most objective planar parallel alignment possible.

For this purpose, the sensor stack is placed close to the glass plate and then pressed against it in 50 µm increments. An image is captured at each increment. These images are evaluated with regard to the center of gravity (CoG) by finding the contact points using a Hough transform and calculating their collective center of gravity. The change in CoG between the images is then calculated. If the position change is less than ± 3pixels in the x and y directions on average for a process, the pad is assumed to be aligned. More information can be found in the Supporting Information and our publication on this experimental procedure [27].

The procedure for recording the calibration curves is similar to that for alignment, except that instead of a defined number of steps, the experiment is repeated with a target force of 60 N, keeping the step size for the calibration curves at 100 µm. It is important to note here that activated pads cause greater shear forces in the system, resulting in a preferred direction within the system. Since the shear forces are related to robot kinematics, there is always a shear force in the direction of the robot base for the Meca 500R3, which also has an effect on the sensor signal, as it influences the deformation behavior of the entire stack. It is therefore important to always calibrate with the robot and that the gripping process always takes place in a defined manner relative to the base. This is an effect that is robot-dependent, as tests carried out on a different robot (Kuka, KR AGILUS sixx) showed. This robot is equipped with mechanisms compensating the shear force and, therefore, the direction dependence does not play a central role for this robot. This effect is described in detail in the Supporting Information.

2.4 | Misalignment

Misalignment experiments can be divided into two categories: on the one hand, misalignment experiments were carried out step by step at a speed of 1 mms^{-1}, on the other hand, the influence of speed was tested, for which three different speeds were tested: 2 mms^{-1}, 5 mms^{-1} and 10 mms^{-1} in continuous driving mode and controlled by distance. For both classes of experiments, the tests were carried out in both the World Reference Frame (WRF) and Tool Reference Frame (TRF) of the robot up to a compression force of 50 N to check whether this has an influence on the results.

2.4.1 | Stepwise Mode

For the first class of tilting experiments with gradual pressing of the sensor, the following seven angle values were tested: 0°, 0.5°, 0.71°, 1°, 1.41°, 1.5°, 2°. The angle values 0.5°, 1°, 1.5° and 2° were considered for rotation around the x or y-axis. The angle values 0.71° and 1.41° are obtained by rotating the sensor around both the x and y axes by 0.5° and 1° respectively. At least the experiments were repeated three times resulting in a total of 151 measurement series for angle detection. Each of these measurement series consists of several hundred thousand individual measurement points.

2.4.2 | Continuous Mode

In order to test the influence of speed on the measurement results, experiments were also conducted in a continuous driving mode with three speed levels (2.5 mm driving distance). For this purpose, the angle values 0°, 0.5°, 1°, 1.5° and 2° were selected and tilted in positive (+) and negative (-) direction around the x or y-axis. At least the experiments were repeated three times resulting in a total of 312 measurement series.

2.5 | Nomenclature Tilting Directions

To facilitate interpretation of the different tilt configurations, Figure 2 illustrates the eight configurations considered in this study. The central panel shows the sensor together with its associated coordinate system, surrounded by the individual tilt configurations. Each circle represents a schematic contact image of the pad, where the highlighted light-gray region indicates the location of first contact for the corresponding tilt. Throughout the paper, the tilt configurations are denoted using the abbreviations +x, -x, +y, -y, +x+y, +x-y, -x+y, and -x-y.

27511219, 2026, 7, Downloaded from https://advanced.onlinelibrary.wiley.com/doi/10.1002/adsr.70172 by Birgit Conrad-Markschläger - Fraunhofer IZFP , Wiley Online Library on [07/07/2026]. See the Terms and Conditions (https://onlinelibrary.wiley.com/terms-and-conditions) on Wiley Online Library for rules of use; OA articles are governed by the applicable Creative Commons License

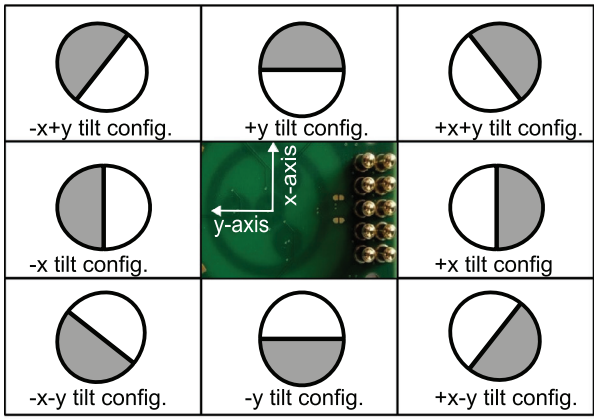

FIGURE 2 | Schematic visualization of the eight different tilting configurations with respect to the sensor's coordinate system.

2.6 | Shape Detection Measurements

The experiments on angular tilt serve as examples of planar geometries and form the basis for object shape detection. A 3D printed test body was used for the curved shaped surface, which had four convex geometries, each with a diameter of 56 mm and radii of 40 mm, 60 mm, 80 mm and 100 mm. The tests are again carried out at a speed of 1 mms^{-1}. The alignment process is performed manually based on the reference coordinates, adjusting the x and y coordinates so that the sensor stack appears to be centered above the shapes. In order to map minor fluctuations, a random x and y offset of ±1 mm is applied to the x and y coordinates so that different non-ideally aligned states are also included. These measurements were also carried out in both the WRF and TRF, resulting in 32 measurement curves for convex geometries.

2.7 | Data Acquisition System

The data acquisition system is built on a STEMlab 125-14 (Red Pitaya) with a custom-written bit file, a custom-made circuit for signal amplification and demodulation and a Raspberry Pi (4) for data processing. The software is uniformly based on Python. A Python server runs on the Red Pitaya for parameterization and control of the FPGA, while a client runs on the Raspberry Pi for communication with the Red Pitaya, where it receives and evaluates the raw data. For easier operation by a user, a web app runs on the Raspberry Pi, for easy parameterization and data collection.

2.8 | Software

The measurement process was controlled by a custom Python software (3.10.5), which synchronized all devices (robot, load cell, sensor, camera, environmental sensors) via the python multiprocessing library. Data analysis and visualization were performed in a separate Python (3.13.10) virtual environment.

2.9 | Statistical Section

2.9.1 | Data Preprocessing

Motivated by the envisioned application of the sensor system as a real-time monitoring device, a rolling mean averaging over 512 data points (multiplex data size) was implemented in the pipeline, as this is faster than software low pass filtering. Data is then offset shifted to be zero at the initial state. For determining positive and negative signal values, the phase between the I and Q channels is calculated.

2.9.2 | Data Presentation

Continuous variables were given as the mean value of the samples, standard deviation (±1 SD) were provided in tables and specific diagrams.

2.9.3 | Sample Size

The sample sizes for the three different experiments are listed:

1. Misalignment evaluation stepwise Mode: 151 measurement series, around 12 million samples.
2. Misalignment evaluation continuous Mode: 312 measurement series, around 1 million samples.
3. Shape prediction: 32 measurement series, around 2 million samples.

Software used for statistical analysis: Python was used throughout the analysis. Mostly used libraries for data analysis: NumPy, Pandas, SciPy, Open-CV2, scikit-learn. For data visualization: Matplotlib and Open-CV2. Code for angle and shape prediction were optimized using ChatGPT 4o (accessed July, December 2025) as well as data visualization was improved via ChatGPT 5.2 (accessed September 2025) code generation. All AI-generated code was reviewed, tested, and revised by the authors, who confirmed accuracy and reproducibility of results.

3 | Results and Discussion

This research presents a newly developed tactile coil-based sensor for misalignment detection of microstructured adhesive pads, with design features enabling generalization from planar to convex surfaces. In addition, evaluations are carried out with industry-oriented adhesive pads designed for maximum adhesive force. First, the working principle is presented. Second, the upgraded data acquisition system is presented. This is followed by the measurement results regarding calibration, misalignment detection and predicting of object shape.

3.1 | Working Principle

The sensor's operating principle is based on eddy currents induced in the conductive layer by the transmitting coil and sensed by the receiver coils. As the distance between the con-

27511219, 2026, 7, Downloaded from https://advanced.onlinelibrary.wiley.com/doi/10.1002/adsr.70172 by Birgit Conrad-Markschläger - Fraunhofer IZFP , Wiley Online Library on [07/07/2026]. See the Terms and Conditions (https://onlinelibrary.wiley.com/terms-and-conditions) on Wiley Online Library for rules of use; OA articles are governed by the applicable Creative Commons License

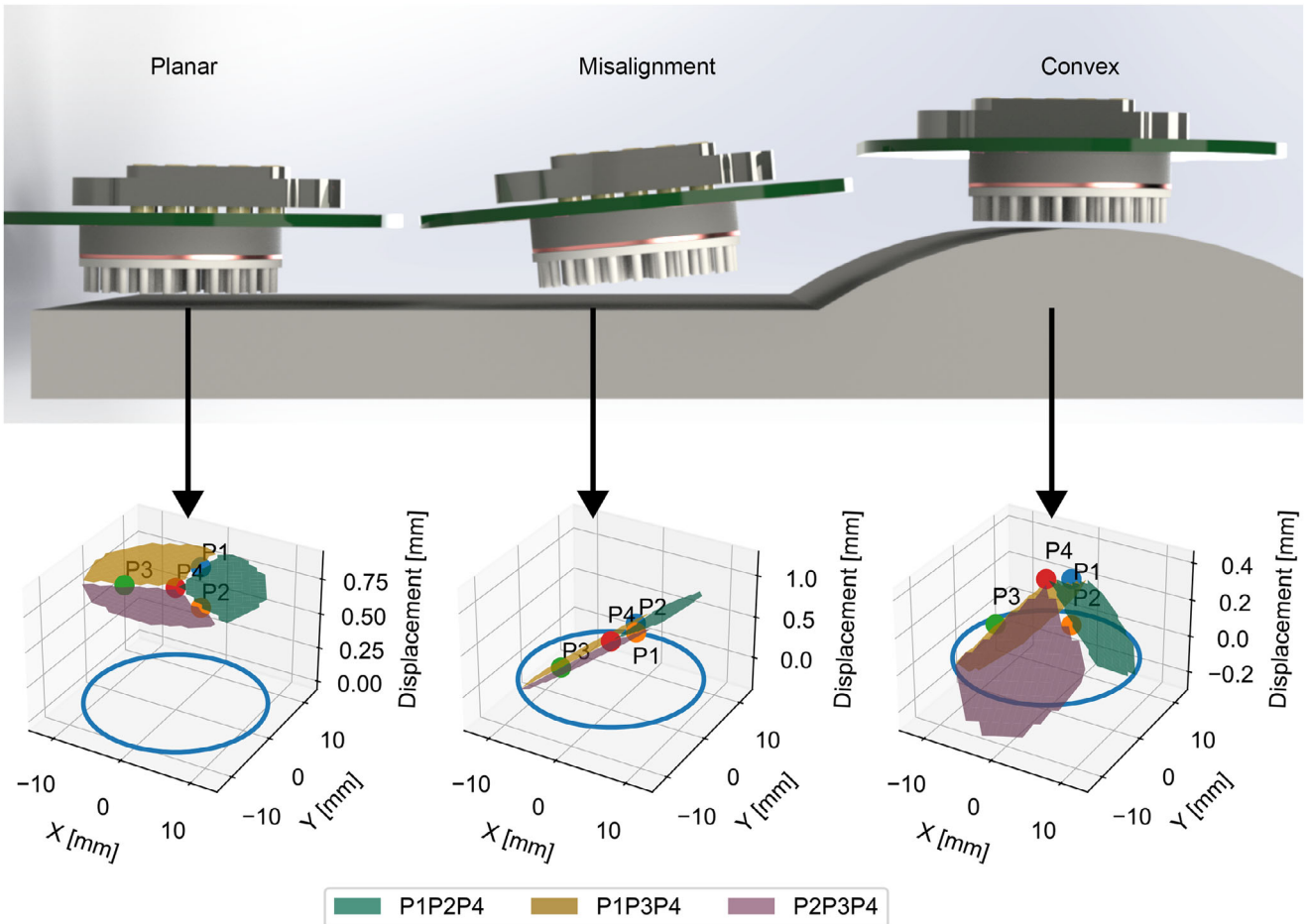

FIGURE 3 | Measurements of aligned, misaligned and convex shapes visualized for each receiver coil as points in 3D space complemented by the three planes (P1P2P4, P1P3P4, P2P3P4) from the four points over the limited area of the sensor's diameter of 24 mm (blue circle). The measured displacement corresponds to the relative compressive deformation of the foam.

ductive layer and the coils changes, the induced voltage in the receiving coils changes. This is the primary measuring effect of the sensor. To maximize the dynamics of the system, in-phase and quadrature (IQ) demodulation is applied on the custom-built analog electronic card. A special feature is that each channel can be offset-corrected separately via a digital potentiometer, which allows differences in the properties of the coils or sensor stack to be compensated for. The transmission frequency is set to 3 MHz, as this enables a phases between 130° to 145° when aligned. To facilitate understanding of the sensor signals and their behavior across different measurement scenarios, Figure 3 illustrates representative cases for planar objects in aligned and misaligned configurations, as well as for convex objects.

The fundamental measurement principle converts the electrical sensor signals into distance changes using calibration coefficients. These distances are then represented in three-dimensional space, forming a characteristic signature of the object. The angular orientation is determined by fitting a plane to the four measured points via singular value decomposition (SVD).

Due to the tilting of the conductive material and the robot kinematics, the sensor shows a phase shift, resulting in discontinuities considering the signal amplitude. To avoid these discontinuities, the amplitude is not calculated from the I and Q channels as usual, but both channels are calibrated individually, providing one continuous signal channel Q and one discontinuous channel I.

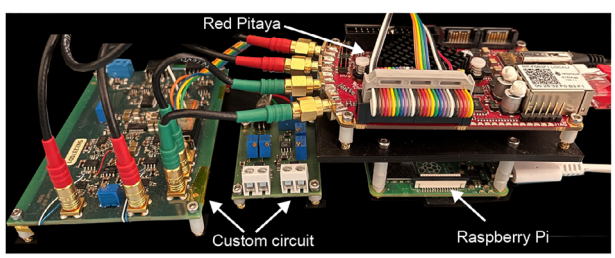

FIGURE 4 | Image of the measuring system. On the left side, the custom circuit responsible for signal amplification and demodulation is shown. On the right-hand side, the digital part consisting of Red Pitaya and Raspberry Pi are pictured.

3.2 | Data Acquisition System

The system has been expanded to include a Raspberry Pi 4 for data processing, shown in Figure 4. Overall, it consists of three dedicated components: the Red Pitaya as an FPGA board for

27511219, 2026, 7, Downloaded from https://advanced.onlinelibrary.wiley.com/doi/10.1002/adsr.70172 by Birgit Conrad-Markschläger - Fraunhofer IZFP , Wiley Online Library on [07/07/2026]. See the Terms and Conditions (https://onlinelibrary.wiley.com/terms-and-conditions) on Wiley Online Library for rules of use; OA articles are governed by the applicable Creative Commons License

signal generation and reception, the custom-made circuit for signal demodulation and amplification, and the Raspberry Pi for data processing.

By separating the data processing hardware and the signal generation hardware, higher data rates are achievable which are often necessary in robot control systems. The updated system runs at 618.6 Hz. Moreover, the system can also be adapted to different hardware platforms in a modular fashion by replacing the Raspberry Pi with the required hardware.

3.3 | Calibration Measurements

First, the sensor is aligned according to the procedure described in Section 2.3. From these initial coordinates calibration is performed by stepwise compressing the sensor stack in increments of 100 µm until a maximum force of 60 N is reached. This procedure is repeated four times to ensure repeatability. During calibration, the sensor signals, step index, and simultaneously measured force are synchronized using Python multiprocessing and stored as a single data set.

As described in Section 3.1, the I and Q channels are processed independently to calculate the displacement. The sensor stack is calibrated as complete assembly (PCB, deformable layer, sensing layer, pad), which ensures that alignment errors in the assembly of the individual components and the geometry of the adhesive pads with modified tip geometry are inherently accounted for.

In the experiments, no direct reference for displacement is available as the system comprises two compliant materials (foam and pad). Consequently, displacement cannot be measured directly and instead must be inferred from the known force-displacement curve of the foam, or alternatively estimated using a scaling factor as reported in Ref. [27]. Since force is recorded simultaneously during measurement, the foam force-displacement curves are used in this work to determine the corresponding displacement at a given force.

During calibration, the foam force-displacement curve (Figure 5a) is combined with the coil signal displacement (Figure 5b). By synchronizing the force values of both measurements, the corresponding displacement signal curves are obtained and used for calibration (Figure 5c).

Selecting an appropriate fitting curve is crucial for sensor calibration. To this end, first, second, and third-order polynomials were evaluated. The second- and third-order polynomials provided a reasonable representation within the calibration range. However, the cubic polynomial exhibits inflection points relatively quickly, including one in the negative domain. This behavior is not physically reasonable, since increasing compression should lead to a monotonically increasing response without inflection. Therefore, a quadratic polynomial was chosen in this work, with the additional constraint that the intercept is fixed at 0. Because at ideal conditions, the absence of contact implies zero displacement and, consequently, a zero sensor output. The curve_fit function from SciPy is used for this purpose, with the polynomial function $(ax^2 + bx)$. Calibration coefficients are not averaged across multiple measurement series. Instead, the measurement series are combined into a calibration data set. The coefficient of determination R^2 and the root mean square error (RMSE) are considered as statistical validation of the coefficients found. This results in the following individual calibration coefficients for the I (see Table 1) and Q channel (see Table 2).

TABLE 1 | Calibration coefficients of each receiver coil regarding the I channel.

Receiver	a [µm digit^{-2}]	b [µm digit^{-1}]	RMSE [µm]	R^2
Coil1	1.13e-07	0.021	28.17	0.9918
Coil2	5.55e-07	0.011	19.46	0.9961
Coil3	5.18e-07	0.018	19.54	0.9961
Coil4	3.96e-08	0.022	29.08	0.9913

TABLE 2 | Calibration coefficients of each receiver coil regarding the Q channel.

Receiver	a [µm digit^{-2}]	b [µm digit^{-1}]	RMSE [µm]	R^2
Coil1	1.71e-07	0.020	29.03	0.9913
Coil2	3.41e-07	0.010	21.55	0.9952
Coil3	6.55e-07	0.028	19.98	0.9959
Coil4	6.51e-08	0.022	28.50	0.9916

According to Table 1 and Table 2, each coil has a coefficient of determination of at least $R^2 = 0.99$. Such high coefficient of determinations indicate an excellent model fit. In addition, the RMSE values for both channels range from 19 µm to 29 µm, translating to a maximum relative error of about 3 % for a measurement interval up to approximately 920 µm. Considering the behavior of the foam, which has an average deviation of approximately 35 µm at 50 cycles, the RMSE is the range of materials fluctuation.

Using the values from Tables 1 and 2, the displacement for the I and Q channels is calculated individually. Nevertheless both channels are required for sign determination via phase calculation. For negative signal values the quadratic calibration curve gets extrapolated, for details see Supporting Information.

3.4 | Sensor Validation

The sensor system is validated in terms of misalignment detection in several spatial directions (see Figure 2) and in terms of its ability to distinguish between flat and convex surfaces.

3.4.1 | Misalignment

For each channel (I and Q), the spatial misalignment is estimated independently by fitting a common plane via singular value decomposition (SVD) to the four 3D points measured by the receiver coils (P1–P4). The calculated plane vector gets compared to a reference vector $\mathbf{r} = [0,0,-1]$ to calculate the misalignment angle.

27511219, 2026, 7, Downloaded from https://advanced.onlinelibrary.wiley.com/doi/10.1002/adsr.70172 by Birgit Conrad-Markschläger - Fraunhofer IZFP , Wiley Online Library on [07/07/2026]. See the Terms and Conditions (https://onlinelibrary.wiley.com/terms-and-conditions) on Wiley Online Library for rules of use; OA articles are governed by the applicable Creative Commons License

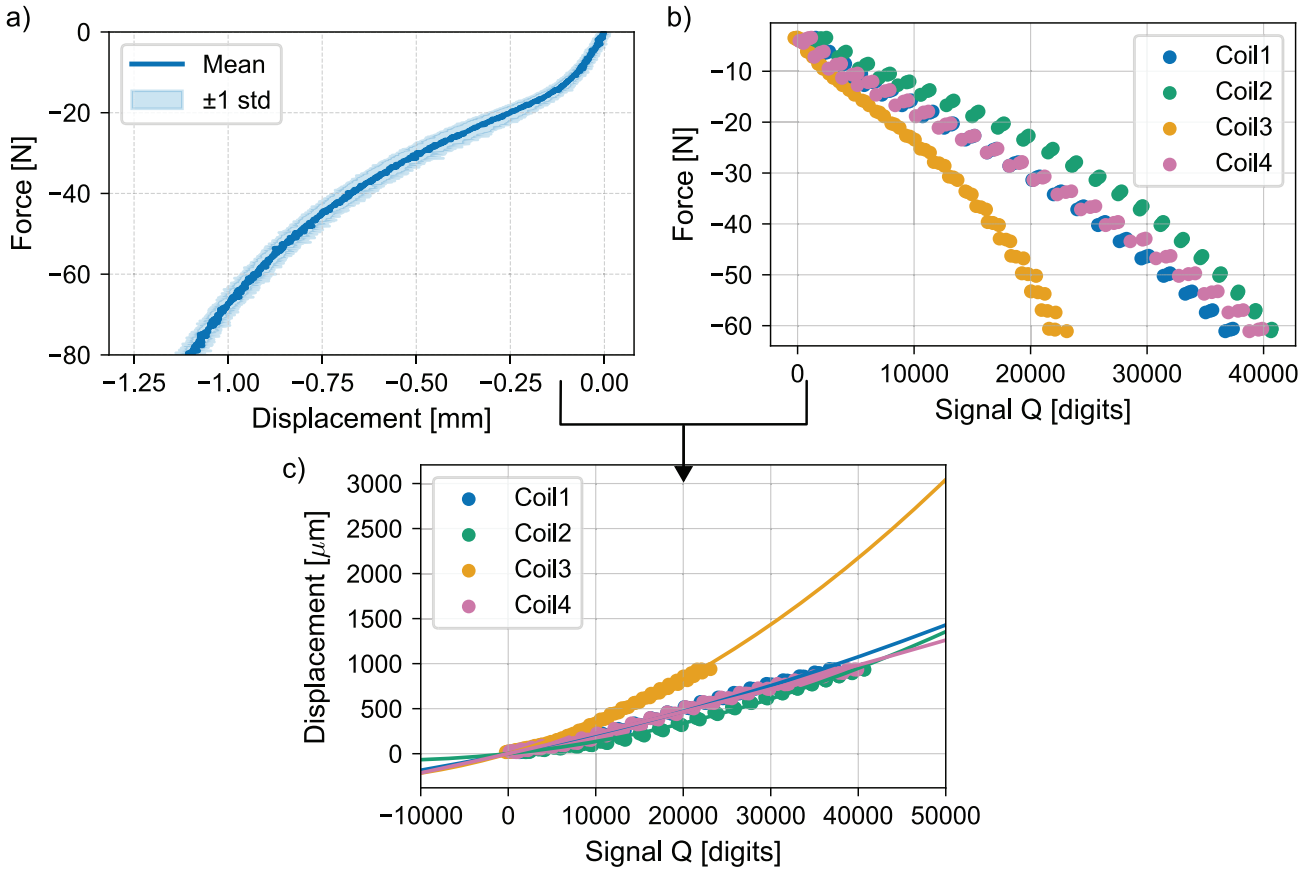

FIGURE 5 | Calibration procedure for fully assembled sensor stack exemplified for channel Q: (a) force-displacement curve of the foam in compression with standard deviation, (b) example of force-signal curve for one of the receiver coils, (c) calculated displacement-signal curve from synchronized data from (a) and (b).

For clarity, Figure 6a illustrates the coil together with its local coordinate system and the positions of the four receiver coils (P1–P4). When the sensor is misaligned, the individual receiver coils experience different sensing distances (S1, S2, S3), depending on the direction of the tilt. These sensing distances must be related to the effective measuring distance, as the sensor comes into contact at an angle and the edges of the pad touch first.

To account for this effect, a scaling factor is introduced in the angle calculation. The sensing distances are averaged and set in relation to the measuring distance, as shown in Figure 6b, which illustrates angled contact and the corresponding measuring distance. The resulting quotient of sensing distance to measuring distance compensates for the geometric discrepancy. For the given sensor layout, this scaling factor is approximately 2.25, see Equation (1).

$$scalingFactor = \frac{Measuring\ distance}{Sensing\ distance} = \frac{24\,\mathrm{mm}}{S1 + S2 + S3} \quad (1)$$

The angle calculation is based on the assumption of planar misaligned surfaces. As the system is soft, sufficient contact pressure is required until the sensor detects the plane to be mapped. Nevertheless, the system continuously provides data, including both the quantified misalignment angle and the corresponding direction. During the contact process, the estimated misalignment angle increases as compression progresses and gradually converges during the measurement. Because the system is calibrated only up to a maximum compression of 920 μm, angle estimation is restricted to this range. Consequently, for large misalignment angles, full convergence may not always be achieved within a single measurement. To ensure a robust prediction under these conditions, the maximum angle observed over the entire measurement sequence is taken as the final predicted misalignment angle. For clarity, Figure 7a shows a raw measurement of the four receiver coils (P1–P4), while Figure 7b presents the corresponding predicted angle as a function of the samples acquired during the stepwise measurement.

To quantify misalignment detection and validate the sensor, it is tilted in both the positive (+) and negative (-) directions around the x and y-axis in two reference systems the TRF and the WRF. Subsequently, it is also tilted around the x and y-axis simultaneously to rule out directional dependence of the sensor. Validation is performed separately for both I and Q channel. The abbreviations of the tilting configurations in this section follow the nomenclature presented in Section 2.5.

For the analysis of the I channel, results are summarized in Tables 3 and 4 for WRF and TRF reference systems, respectively. The maximum absolute error is 0.58 ° with a RMSE of 0.32 ° in WRF and 0.59 ° with a RMSE of 0.34 ° for TRF. For the aligned

27511219, 2026, 7, Downloaded from https://advanced.onlinelibrary.wiley.com/doi/10.1002/adsr.70172 by Birgit Conrad-Markschläger - Fraunhofer IZFP , Wiley Online Library on [07/07/2026]. See the Terms and Conditions (https://onlinelibrary.wiley.com/terms-and-conditions) on Wiley Online Library for rules of use; OA articles are governed by the applicable Creative Commons License

TABLE 3 | Angle evaluation for tilting around the x and y-axis for channel I moving in WRF.

Reference angle [°]	x [°]	-x [°]	y [°]	-y [°]	SD x [°]	SD -x [°]	SD y [°]	SD -y [°]
0.5	0.9	0.87	0.6	0.71	0.03	0.03	0.02	0.02
1	1.58	1.54	1.13	1.22	0.01	0.02	0.03	0.03
1.5	2.04	1.95	1.67	1.69	0.02	0.01	0.01	<0.01
2	2.15	2.12	2.07	2.07	0.02	0.01	0.01	0.03

TABLE 4 | Angle evaluation for tilting around the x and y-axis for channel I moving in TRF.

Reference angle [°]	x [°]	-x [°]	y [°]	-y [°]	SD x [°]	SD -x [°]	SD y [°]	SD -y [°]
0.5	0.97	0.84	0.75	0.63	0.03	<0.01	0.02	0.01
1	1.58	1.44	1.28	1.19	0.01	<0.01	0.03	<0.01
1.5	2.09	2	1.8	1.74	0.05	0.01	0.02	0.01
2	2.12	2.2	2.06	2.01	0.04	0.02	0.03	0.03

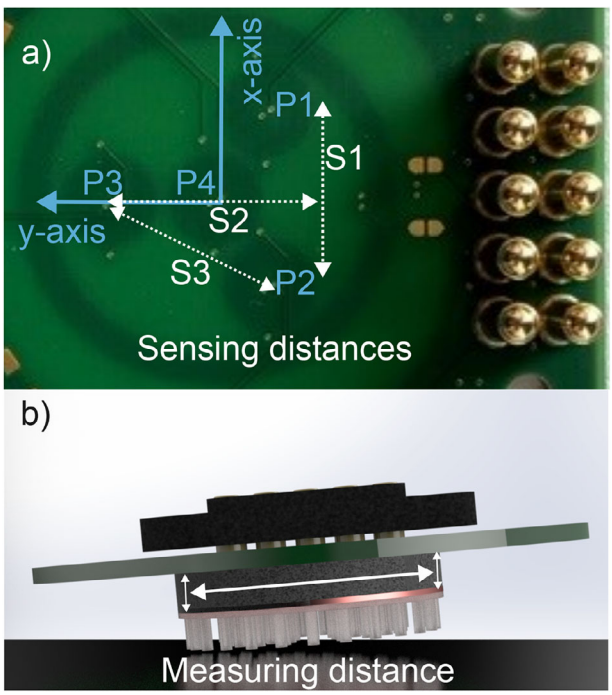

FIGURE 6 | (a) Image of the sensor coils with coordinate system and the sensing position P1, P2, P3 and P4 for the four receiver coils and the sensing distances S1, S2 and S3. (b) Illustration of the measuring distance for tilted configuration.

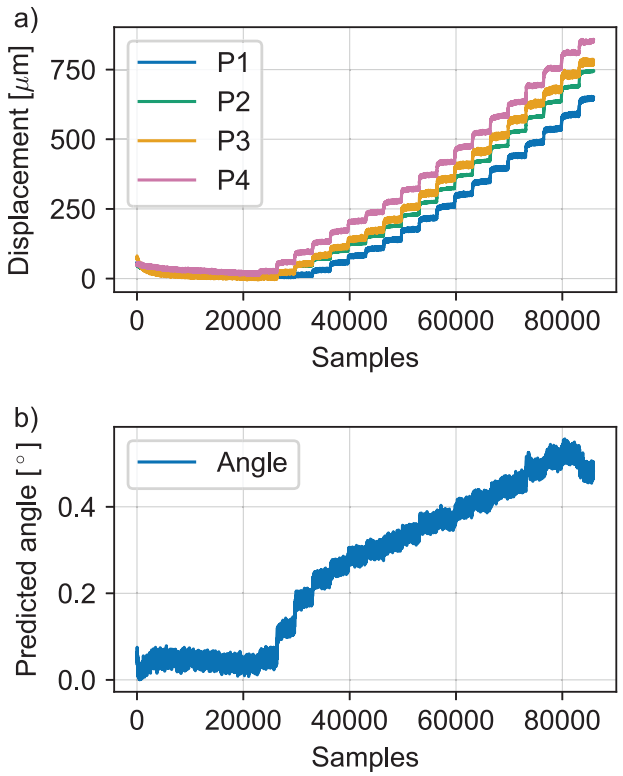

FIGURE 7 | Measurement plots: (a) Displacement measurements of the four receiver coils P1 to P4, (b) Predicted angle over samples.

state (reference angle = 0 °) the measured mean misalignment angles for the I channel are 0.23 ° in the WRF and 0.26 ° in the TRF. So overall there is no difference in moving the sensor in different reference system which should be the case and is proofed.

Tables 5 and 6 below summarize the maximum angles recorded for different misalignments around the x and y-axis based on the two reference systems (WRF, TRF) for the Q channel. The highest absolute error is 0.32 ° with an overall RMSE of 0.18 ° for moving the sensor in WRF and 0.26 ° with a RMSE of 0.15 ° for TRF. For the aligned state (reference angle = 0 °) the measured mean angle for the Q channel is 0.17 ° when referenced to the WRF and 0.19 ° when referenced to the TRF. As for the I channel, moving in a different reference system is not affecting the measurement precision as results are quite close. However, the data from I channel shows higher error nearly doubled in absolute error and also RMSE. Consequently, only data from the Q channel are used for further angle analysis, as this channel exhibits higher

27511219, 2026, 7, Downloaded from https://advanced.onlinelibrary.wiley.com/doi/10.1002/adsr.70172 by Birgit Conrad-Markschläger - Fraunhofer IZFP , Wiley Online Library on [07/07/2026]. See the Terms and Conditions (https://onlinelibrary.wiley.com/terms-and-conditions) on Wiley Online Library for rules of use; OA articles are governed by the applicable Creative Commons License

TABLE 5 | Angle evaluation for tilting around the x and y-axis for channel Q moving in WRF.

Reference angle [°]	x [°]	-x [°]	y [°]	-y [°]	SD x [°]	SD -x [°]	SD y [°]	SD -y [°]
0.5	0.68	0.73	0.5	0.56	0.05	0.04	0.03	0.01
1	1.17	1.29	0.92	0.97	0.04	0.01	0.02	0.04
1.5	1.63	1.72	1.34	1.35	0.05	0.01	0.01	0.04
2	2	2.02	1.69	1.68	0.03	<0.01	0.02	0.03

TABLE 6 | Angle evaluation for tilting around the x and y-axis for channel Q moving in TRF.

Reference angle [°]	x [°]	-x [°]	y [°]	-y [°]	SD x [°]	SD -x [°]	SD y [°]	SD -y [°]
0.5	0.72	0.76	0.62	0.51	0.01	0.01	0.01	<0.01
1	1.16	1.22	1.06	0.97	0.01	0.01	0.01	0.01
1.5	1.66	1.70	1.45	1.39	0.02	<0.01	0.03	<0.01
2	1.99	2	1.82	1.91	0.04	0.02	0.01	0.01

TABLE 7 | Angle evaluation for tilting around the x and y-axis simultaneously for Q channel moving in WRF.

Reference angle [°]	+x+y [°]	-x+y [°]	-x-y [°]	+x-y [°]	SD +x+y [°]	SD -x+y [°]	SD -x-y [°]	SD +x-y [°]
0.71	0.87	0.79	0.73	0.83	0.02	0.01	0.01	0.01
1.41	1.58	1.36	1.38	1.45	0.02	0.02	0.02	0.01

precision. This behavior is expected, since the I channel is more strongly affected by the phase effects described. Nevertheless, the I channel data remain essential to determine the angle sign during the measurement.

In order to evaluate the sensor system independently of the tilt directions, it is necessary to examine how the angle prediction behaves when tilted around the x and y-axis simultaneously. To achieve this, the sensor was rotated around both axes by 0.5° and 1° respectively, resulting in a tilt of approximately 0.71° and 1.41°. The following Tables 7 and 8 show the results for tilting around x and y-axis simultaneously. For moving in WRF the highest absolute error is 0.17° and the RMSE is 0.1°. The highest absolute error for moving in TRF is 0.26° and the RMSE is 0.14°. Again, the difference between the moving system are marginal and the errors are in similar range to tilting just around one axis. No directional dependence is observed, and similar accuracy is achieved for all tilt configurations.

The results for the predicted angle are summarized based on the data from channel Q in Figure 8, indicating a linear correlation between the predicted and the reference tilt angle, for easier visibility the plot contains the absolute angle value with no differentiation of the tilt direction.

3.4.1.1 | Verification of Tilt Directions. For the feedback loop in the control process, the direction of the tilt rather than the magnitude of tilt is the main parameter for adapting the gripping process. For this purpose, the calculated vector was projected onto a 2D plane. An illustration of the determined directions for the different experiments carried out is shown in Figure 9 for channel Q. As shown in the graph 9a and b, the tilt direction can be reliably detected as the projected vectors point toward the correct axis in the coordinate system.

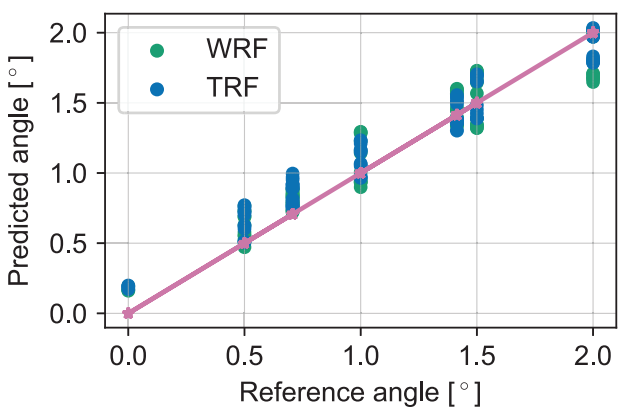

FIGURE 8 | Predicted angle vs. reference angle curve.

3.4.1.2 | Misalignment Measurements at Different Velocities. Angle prediction must also be tested at different velocities to verify the reliability of the system as described in Section 2.4. Results are listed in Table 9 whereby the angles are not sorted according to misalignment direction this time, but are shown as the average value over the respective angle value. Regardless of the velocity, the angle predictions are comparable. Even the standard deviations, which in this case are higher than those of the previous evaluations, show comparable value

27511219, 2026, 7, Downloaded from https://advanced.onlinelibrary.wiley.com/doi/10.1002/adsr.70172 by Birgit Conrad-Markschläger - Fraunhofer IZFP , Wiley Online Library on [07/07/2026]. See the Terms and Conditions (https://onlinelibrary.wiley.com/terms-and-conditions) on Wiley Online Library for rules of use; OA articles are governed by the applicable Creative Commons License

TABLE 8 | Angle evaluation for tilting around the x and y-axis simultaneously for Q channel moving in TRF.

Reference angle [°]	+x+y [°]	-x+y [°]	-x-y [°]	+x-y [°]	SD +x+y [°]	SD -x+y [°]	SD -x-y [°]	SD +x-y [°]
0.71	0.83	0.97	0.76	0.91	0.05	0.02	0.01	0.01
1.41	1.35	1.54	1.37	1.5	0.04	0.01	0.01	0.01

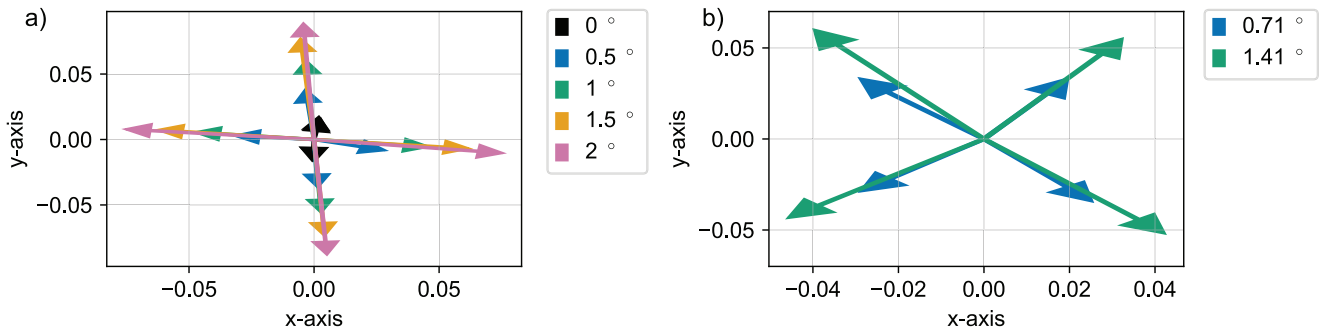

FIGURE 9 | Arrow plot of detect misalignment direction from normalized vector projections: (a) Misalignment directions for tilting around x or y-axis, (b) Misalignment directions for tilting around x and y-axis simultaneously.

TABLE 9 | Angle evaluation for tilting around the x and y-axis simultaneously for Q Channel.

Velocity [mms^{-1}]	Reference angle [°]	Pred. angle WRF [°]	SD WRF [°]	Pred. angle TRF [°]	SD TRF [°]
2	0	0.24	0.02	0.3	0.02
2	0.5	0.65	0.13	0.65	0.16
2	1	1.12	0.2	1.14	0.16
2	1.5	1.57	0.21	1.59	0.16
2	2	1.92	0.2	1.96	0.13
5	0	0.27	<0.01	0.31	0.01
5	0.5	0.66	0.15	0.65	0.17
5	1	1.12	0.2	1.14	0.15
5	1.5	1.56	0.2	1.60	0.16
5	2	1.92	0.19	1.97	0.14
10	0	0.27	0.01	0.29	0.01
10	0.5	0.66	0.15	0.65	0.16
10	1	1.12	0.19	1.14	0.14
10	1.5	1.56	0.19	1.6	0.16
10	2	1.92	0.18	1.97	0.14

ranges among the different velocities. The standard deviations are higher because they were calculated over the rotations of the different axes. It is therefore important to include the mean error for the measurements. The RMSE in the WRF is approximately 0.21 ° and in the TRF it is also 0.21 °. It is important to note that the highest absolute errors are 0.4 ° in the WRF and 0.35 ° in the TRF. The evaluations show a similar picture to the data recorded step by step, which have an RMSE of approximately 0.18 ° and a maximum error of 0.32 °. It can be seen that the RMSE differs by only 0.03 ° and the absolute error by 0.08 °, so the functionality of the system can also be determined at significantly higher working velocities.

Figure 10 presents the temporal prediction for a reference angle of 1 ° at two different velocities in panel a. Panel b shows the predicted angles relative to the reference angle for three different velocities: 2 mms^{-1}, 5 mms^{-1}, and 10 mms^{-1}. An example of the detected misalignment directions at 10 mms^{-1} is shown in panel c.

Figure 10 demonstrates that the sensor's sampling rate is sufficient for reliable angle prediction at velocities of up to 10 mms^{-1}. As shown in panel a, more than 100 samples are acquired during a contact process lasting approximately 0.25 s at 10 mms^{-1}, and more than 700 samples are recorded over a duration of

27511219, 2026, 7, Downloaded from https://advanced.onlinelibrary.wiley.com/doi/10.1002/adsr.70172 by Birgit Conrad-Markschläger - Fraunhofer IZFP , Wiley Online Library on [07/07/2026]. See the Terms and Conditions (https://onlinelibrary.wiley.com/terms-and-conditions) on Wiley Online Library for rules of use; OA articles are governed by the applicable Creative Commons License

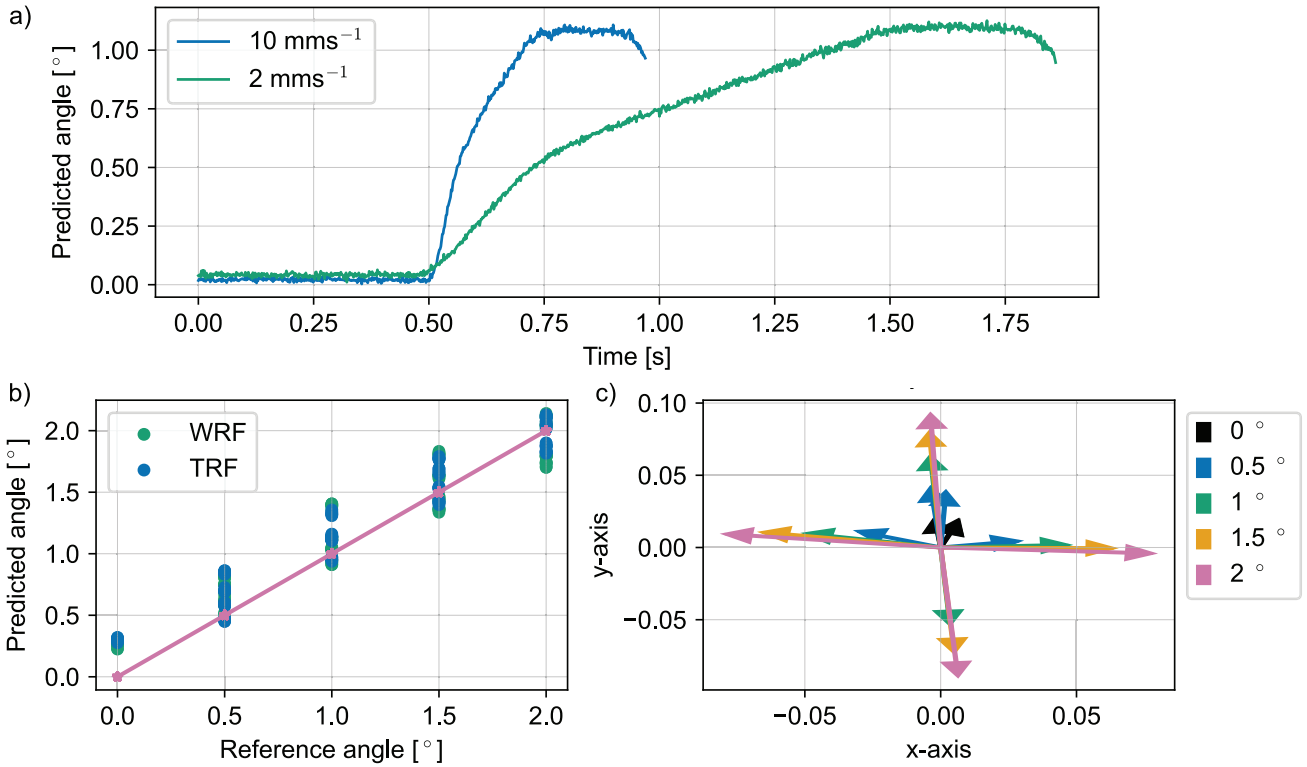

FIGURE 10 | Measurement plots: (a) Example of predicted angles over time for measurements at 2 mms^{-1} and 10 mms^{-1}, (b) Predicted Angle over reference angle for velocities of 2 mms^{-1}, 5 mms^{-1} and 10 mms^{-1}, (c) Tilting directions shown exemplarily for a velocity of 10 mms^{-1} in WRF and the four different tilting configurations plus the aligned state.

about 1.25 s at a velocity of 2 mms^{-1}. Panel b confirms a linear correlation between velocity and sampling behavior, while panel c demonstrates reliable detection of the misalignment direction along the respective axes.

3.4.2 | Shape Prediction

In order to distinguish between planar and convex curved surfaces, the first step is to calculate features that enable distinction between the object shapes. An object shape can be approximated in 3D space based on the four receiver signals (P1, P2, P3, P4) by calculating three surfaces between the point pairs (P1, P2, P4) (P1,P3,P4) and (P2,P3,P4) above the sensor surface (Figure 11 blue circle). Figure 11 shows the three fitted planes through the point triplets from a convex measurement of sample with 40 mm radius. The middle coil senses the most displacement and the shape is looking convex. The blue circle indicates the outlines of the sensor and is provided to guide the eyes of the reader.

Based on these considerations, the signed distances of the four measured points to their best-fitting plane (obtained via SVD) are calculated. For a convex surface, the central point (receiver P4) is expected to lie above the plane, while the remaining points lie below it, resulting in a characteristic convex configuration. This yields four distance-based features, defined as the signed distances of receiver points P1–P4 to the best-fitting plane, denoted as DP1, DP2, DP3 and DP4. In addition, the sphericity of the point distribution (P1-P4) is quantified using SVD of the four

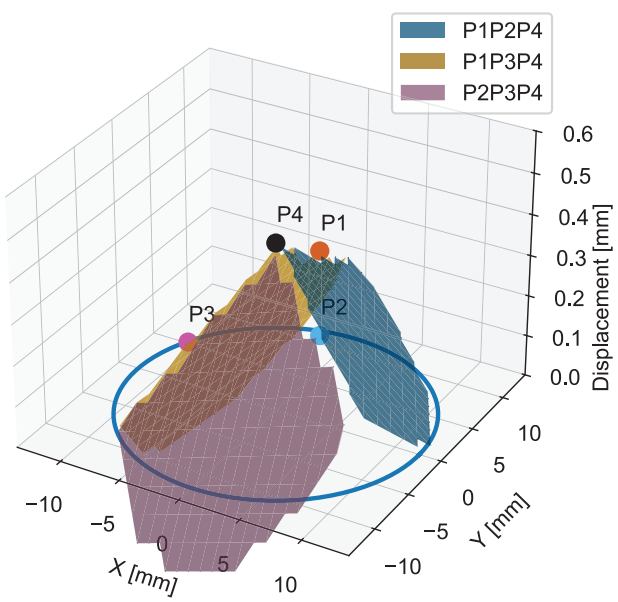

FIGURE 11 | 3D plot of reconstructed surfaces from a measurement on a spherical sample with radius 40 mm.

receiver points (P1-P4). The eigenvalues $\lambda 1, \lambda 2$ and $\lambda 3$ obtained from the SVD are used to compute the sphericity according to Equation (2), providing an additional shape descriptor.

$$sphericity = \lambda 3/\lambda 1 \tag{2}$$

27511219, 2026, 7, Downloaded from https://advanced.onlinelibrary.wiley.com/doi/10.1002/adsr.70172 by Birgit Conrad-Markschläger - Fraunhofer IZFP , Wiley Online Library on [07/07/2026]. See the Terms and Conditions (https://onlinelibrary.wiley.com/terms-and-conditions) on Wiley Online Library for rules of use; OA articles are governed by the applicable Creative Commons License

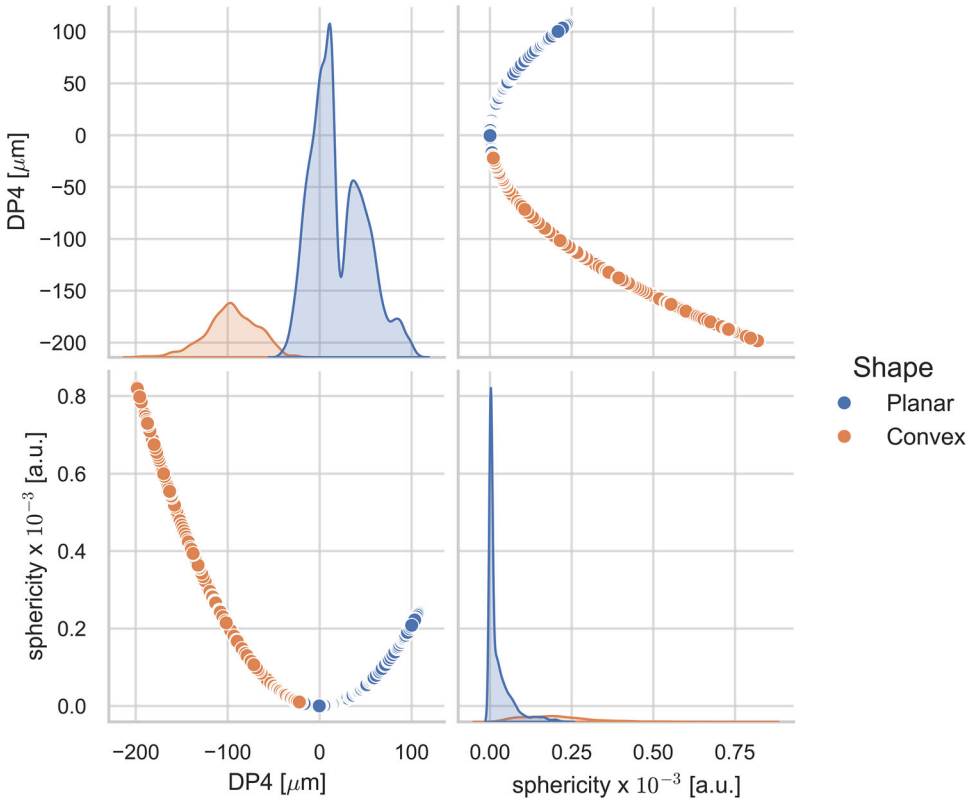

FIGURE 12 | Pairplot of the two extracted features sphericity and signed distance of coil 4.

The five characteristics (DP1, DP2, DP3, DP4, sphericity) mentioned above are used to train a classifier that is capable of separating the two classes. To get an overview of how these features divide the data into classes of planar and convex surfaces, the sphericity and distance feature of the middle coil (DP4) are shown as an example in Figure 12.

Similar to angle predictions, the object shape evaluation requires sufficient deformation of the sensor. A displacement of 200 µm from the mean of all receiversis set as a sufficient limit to predict the shape.

To classify the data, the k-nearest neighbors (kNN) classifier was selected as basis for the predictive model. This method offers a straightforward prediction strategy based on distances.

Because the data samples consist of time-series measurements, the validation strategy requires careful selection. Applying k-fold cross-validation would randomly distribute samples across training and test sets, introducing information leakage. In particular, samples originating from the same measurement sequence could appear in both sets, artificially improving performance metrics. To avoid this issue, a leave-one-group-out (LOGO) cross-validation strategy is employed [29, 30].

3.4.2.1 | Dataset and Results. The data set comprises stepwise angle measurements on planar surfaces, as described in Section 2.4, as well as measurements on convex surfaces from Section 2.6. These data form seven groups for the planar class, corresponding to individual test angles, and four groups for the convex class, corresponding to the tested objects. In total, the data set includes 183 measurements comprising several million samples. The results of the leave-one-group-out (LOGO) validation for the individual groups are summarized in Table 10.

TABLE 10 | Results of the leave-one-group-out validation.

Group	Accuracy [%]	Samples	Misclassifications
Planar 2 °	99.96	374884	137
Planar 1.5 °	100	528101	0
Planar 1.4 °	100	489536	0
Planar 1 °	100	688130	0
Planar 0.7 °	100	760214	0
Planar 0.5 °	100	862402	0
Planar 0 °	100	294840	0
Convex 100 mm	100	155490	0
Convex 80 mm	97.41	214516	5566
Convex 60 mm	100	209936	0
Convex 40 mm	99.94	183060	118

Each group comprises multiple measurements, within which the data retain a temporal structure. Consequently, it is necessary to examine groups exhibiting classification errors in greater detail, as the temporal behavior of individual measurements and the distribution of errors across them are critical for interpretation. The analysis reveals that misclassifications do not occur consistently across a group but are confined to specific measurements. As can

27511219, 2026, 7, Downloaded from https://advanced.onlinelibrary.wiley.com/doi/10.1002/adsr.70172 by Birgit Conrad-Markschläger - Fraunhofer IZFP , Wiley Online Library on [07/07/2026]. See the Terms and Conditions (https://onlinelibrary.wiley.com/terms-and-conditions) on Wiley Online Library for rules of use; OA articles are governed by the applicable Creative Commons License

be seen in Table 10 only three groups (planar 2°, convex 80 mm and convex 40 mm) show misclassifications.

In the planar 2° condition, all misclassifications are confined to a single measurement, resulting in an overall accuracy of 99.27 % with 137 misclassified samples. A similar concentration of errors is observed for the convex 80 mm condition, where misclassifications occur in two out of eight measurements. One of these measurements achieves an accuracy above 99.99 %, with only a single misclassified sample, whereas the other exhibits 5565 misclassifications, corresponding to an accuracy of 73.81 %. The observed decrease in accuracy is associated with a mechanical instability phenomenon, such as buckling, as evidenced by the recorded force data and the receiver signals, both of which exhibit an abrupt reduction in magnitude. Smaller radii are expected to promote buckling-like effects because the effective contact area is reduced by geometric constraints. Under buckling, the microstructure of the adhesive pads undergoes bending or out-of-plane deformation, which can result in ambiguous or unreliable signal acquisition. In contrast, the convex 40 mm condition shows misclassifications in three out of eight measurements. However, each of these measurements maintains an accuracy exceeding 99.5 %, with a maximum of 63 misclassified samples.

Finally, the data from the velocity tests were also evaluated using this procedure, a total of 312 measurement series, with 133147 samples, on planar objects. All samples, are correctly classified as planar by the proposed kNN model.

As noted previously, the temporal structure of the measurements is known, and the control system is aware of the current measurement cycle. This enables aggregation of the sample-wise classification outputs at the control level and their evaluation as a whole. A majority-based decision criterion can therefore be applied to generate a stable, continuous output. Specifically, a threshold-based approach is employed, in which a reliability threshold of 99 % is defined. A classification result is accepted as reliable only if at least 99 % of the samples within a measurement cycle correspond to the same class. Otherwise, the classification is labeled as ambiguous.

When applied to the complete data set presented in this study, this procedure results in only one out of 495 measurement series being classified as ambiguous.

4 | Conclusion

This paper presents the development of a coil-based sensor which can quantify misalignment angles, directions and classify objects as either planar or convex. The newly developed sensor design provides a plug-and-play solution for numerous robot models thanks to its spring-loaded contacts. System enhancements, including the integration of a Raspberry Pi computing unit and revisions to the analogue electronics, enable high-speed sampling at 618 Hz, meeting the demands of robotic applications. We were able to show that the sensor has no noticeable directional dependencies by testing a total of eight different tilt configurations over an angle range of 0° to 2°. The sensor achieved an average RMSE performance of maximum 0.21°. The largest single angle error that occurred was 0.4°. In addition, different speeds of 2 mms^{-1} to 10 mms^{-1} were also tested with no change in sensor performance, demonstrating the ability to work at higher manipulations velocities. Beyond misalignment detection, the sensor is capable of distinguishing between planar and convex surface geometries. A kNN classifier is employed for object shape prediction and evaluated using a LOGO validation strategy, achieving accuracies between 97 % and 100 % across eleven experimental groups. To further enhance robustness, majority voting across the classifications within each measurement cycle is proposed. A minimum agreement threshold of 99 % is suggested as the decision criterion. With this approach, 494 out of 495 measurement cycles are classified correctly, while one measurement series do not meet the threshold and is therefore labeled as ambiguous. In the future, the system should be expanded, particularly in terms of algorithms, with regard to additional parameters. For example, predicting the contact area as well as the contact pressure in the gripping process is desirable as those factors influence adhesion strength and would enable more versatile control strategies for pick-and-place applications.

Author Contributions

Conceptualization: S.H., Methodology: S.H., Formal analysis: S.H., Funding acquisition: S.C.L.F., In – vestigation: S.H., Supervision: S.C.L.F., Software: S.H., Visualization: S.H., Writing – original draft: S.H., Writing – review and editing: S.H. and S.C.L.F., All authors have read and agreed to the published version of the manuscript.

Acknowledgements

S.H. thanks Jonathan Thiemecke (Innocise GmbH) for his support in adhesions test and designing the quick-change-system. S.H. thanks Philipp Stopp (Fraunhofer IZFP) and Alina Christiana Ehre (HTW Saar) for their help with building and optimizing the custom analog circuit.

Open access funding enabled and organized by Projekt DEAL.

Funding

This research was funded by Federal Ministry of Education and Research as part of the project number 01IS21035B as well as partially funded by a Fraunhofer Internal Program under the Grant No.Attract 025-601314 awarded to S.C.L Fischer. Open access funding enabled and organized by Projekt DEAL.

Conflicts of Interest

The authors declare no conflicts of interest.

Data Availability Statement

The data that support the findings of this study are available from the corresponding author upon reasonable request.

References

1. H. Wang, D. Jones, G. de Boer, et al., "Design and Characterization of Tri-Axis Soft Inductive Tactile Sensors," *IEEE Sensors Journal* 18, no. 19 (2018): 7793–7801.

2. C. Hegde, J. Su, J. M. R. Tan, K. He, X. Chen, and S. Magdassi, "Sensing in Soft Robotics," *ACS Nano* 17, no. 16 (2023): 15277–15307.

3. O. Yasa, Y. Toshimitsu, M. Y. Michelis, et al., "An Overview of Soft Robotics," *Annual Review of Control, Robotics, and Autonomous Systems* 6, no. 1 (2023): 1–29.

27511219, 2026, 7, Downloaded from https://advanced.onlinelibrary.wiley.com/doi/10.1002/adsr.70172 by Birgit Conrad-Markschläger - Fraunhofer IZFP , Wiley Online Library on [07/07/2026]. See the Terms and Conditions (https://onlinelibrary.wiley.com/terms-and-conditions) on Wiley Online Library for rules of use; OA articles are governed by the applicable Creative Commons License

4. A. Dzedzickis, J. J. Petronienė, S. Petkevičius, and V. Bučinskas, "Soft Grippers in Robotics: Progress of Last 10 Years," *Machines* 12, no. 12 (2024): 887, https://www.mdpi.com/2075-1702/12/12/887.

5. L. Wang, J. Xie, S. Wang, et al., "Gecko-Inspired Adhesive Grasping from Convex to Flat Surfaces with Contact Sensing," *Advanced Intelligent Systems* 7, no. 8 (2025): 2400864.

6. E. Arzt, S. Gorb, and R. Spolenak, "From Micro to Nano Contacts in Biological Attachment Devices," *Proceedings of the National Academy of Sciences of the United States of America* 100, no. 19 (2003): 10603–10606.

7. E. Arzt, H. Quan, R. M. McMeeking, and R. Hensel, "Functional Surface Microstructures Inspired by Nature – From Adhesion and Wetting Principles to Sustainable New Devices," *Progress in Materials Science* 120 (2021): 100823.

8. R. G. Balijepalli, S. C. Fischer, R. Hensel, R. M. McMeeking, and E. Arzt, "Numerical Study of Adhesion Enhancement by Composite Fibrils with Soft Tip Layers," *Journal of the Mechanics and Physics of Solids* 99 (2017): 357–378.

9. V. Tinnemann, L. Hernández, S. C. L. Fischer, E. Arzt, R. Bennewitz, and R. Hensel, "In Situ Observation Reveals Local Detachment Mechanisms and Suction Effects in Micropatterned Adhesives," *Advanced Functional Materials* 29, no. 14 (2019): 1807713.

10. E. Kroner, D. R. Paretkar, R. M. McMeeking, and E. Arzt, "Adhesion of Flat and Structured PDMS Samples to Spherical and Flat Probes: A Comparative Study," *Journal of Adhesion* 87, no. 5 (2011): 447–465.

11. K. Suwanratchatamanee, M. Matsumoto, and S. Hashimoto, "Robotic Tactile Sensor System and Applications," *IEEE Transactions on Industrial Electronics* 57, no. 3 (2010): 1074–1087.

12. G. de Maria, C. Natale, and S. Pirozzi, "Force/Tactile Sensor for Robotic Applications," *Sensors and Actuators A: Physical* 175 (2012): 60–72.

13. R. Bhirangi, T. Hellebrekers, C. Majidi, and A. Gupta, "ReSkin: Versatile, Replaceable, Lasting Tactile Skins," *Proceedings of Machine Learning Research* 164 (2021): 587–597, https://arxiv.org/pdf/2111.00071.

14. R. Bhirangi, V. Pattabiraman, E. Erciyes, Y. Cao, T. Hellebrekers, and L. Pinto, "AnySkin: Plug-and-Play Skin Sensing for Robotic Touch," in *2025 IEEE International Conference on Robotics and Automation*, T. Murphey, Ed. (Piscataway, NJ: IEEE, 2025), 16563–16570.

15. V. Pattabiraman, Z. Huang, D. Panozzo, D. Zorin, L. Pinto, and R. Bhirangi, "eFlesh: Highly Customizable Magnetic Touch Sensing Using Cut-Cell Microstructures," (2025), http://arxiv.org/pdf/2506.09994.

16. W. Yuan, S. Dong, and E. H. Adelson, "GelSight: High-Resolution Robot Tactile Sensors for Estimating Geometry and Force," *Sensors* 17, no. 12 (2017): 2762, https://www.mdpi.com/1424-8220/17/12/2762.

17. E. Donlon, S. Dong, M. Liu, J. Li, E. Adelson, and A. Rodriguez, "GelSlim: A High-Resolution, Compact, Robust, and Calibrated Tactile-Sensing Finger," in *Towards a Robotic Society* (Piscataway, NJ: IEEE, 2018), 1927–1934.

18. C. Pang, K. Mak, Y. Zhang, Y. Yang, Y. A. Tse, and M. Y. Wang, "ViKo: An Adaptive Gecko Gripper with Vision-Based Tactile Sensor," in *2021 IEEE International Conference on Robotics and Automation (ICRA)* (IEEE, 2021), 736–742.

19. C. Pang, Q. Wang, K. Mak, H. Yu, and M. Y. Wang, "ViKo 2.0: A Hierarchical Gecko-Inspired Adhesive Gripper with Visuotactile Sensor," *IEEE Robotics and Automation Letters* 7, no. 3 (2022): 7842–7849.

20. I. H. Taylor, S. Dong, and A. Rodriguez, "GelSlim 3.0: High-Resolution Measurement of Shape, Force and Slip in a Compact Tactile-Sensing Finger," in *2022 IEEE International Conference on Robotics and Automation (ICRA)*, M. O'Malley, Ed. (Piscataway, NJ: IEEE, 2022), 10781–10787.

21. B. Mao, K. Zhou, Y. Xiang, et al., "A Bioinspired Robotic Finger for Multimodal Tactile Sensing Powered by Fiber Optic Sensors," *Advanced Intelligent Systems* 6, no. 8 (2024): 2400175, https://onlinelibrary.wiley.com/doi/full/10.1002/aisy.202400175.

22. A. Sipos, W. den van Bogert, and N. Fazeli, "GelSlim 4.0: Focusing on Touch and Reproducibility," (2024), https://arxiv.org/pdf/2409.19770.

23. H. Wang, M. Totaro, and L. Beccai, "Toward Perceptive Soft Robots: Progress and Challenges," *Advanced Science* 5, no. 9 (2018): 1800541.

24. S. Herter, P. Stopp, and S. C. Fischer, "Soft Tactile Coil-Based Sensor for Misalignment Detection of Adhesive Fibrillary Gripping Systems," *Advanced Sensor Research* 3, no. 1 (2024): 2300098.

25. S. Zhang, Y. Xu, X. Chang, et al., "A Fully Integrated, Reconfigurable Multiaxis Force Sensor via Inductive Displacement Sensing," *IEEE Sensors Journal* 24, no. 7 (2024): 9593–9603.

26. Y. Xu, X. Chang, J. Zhang, Y. Wang, and H. Wang, "A Miniature Self-Decoupled Multiaxis Force Sensor via 3D Orthogonal Configuration," in *IEEE Sensors 2024 Conference Proceedings* (Piscataway, NJ, USA: IEEE, 2024), 1–4.

27. S. Herter and S. C. L. Fischer, "Fully Automated Calibration of an Eddy Current Sensor for High-Precision Feedback in Pick-and-Place Applications Using Bioinspired Dry Adhesives," *Technisches Messen* 92, no. s1 (2025): 105–110.

28. T. Li, Y. Wang, Y. Xu, H. Wu, X. Chang, L. Long, and H. Wang, "An Inductive Multimodal Tactile Sensor with a Warm Touch for Human-Like Perception," *IEEE Transactions on Instrumentation and Measurement* 74 (2025): 1–10.

29. P. Goodarzi, A. Schütze, and T. Schneider, "Comparing AutoML and Deep Learning Methods for Condition Monitoring Using Realistic Validation Scenarios," (2023).

30. C. Schnur, P. Goodarzi, Y. Lugovtsova, et al., "Towards Interpretable Machine Learning for Automated Damage Detection Based on Ultrasonic Guided Waves," *Sensors* 22, no. 1 (2022).

Supporting Information

Additional supporting information can be found online in the Supporting Information section.

Supporting File: adsr70172-sup-0001-SuppMat.pdf.

Biographies

Simon Herter graduated from Saarland University in 2020 with a Master of Science degree in materials science. He is currently pursuing a Ph.D. within the MatBeyoNDT research group at Fraunhofer IZFP and the lab for measurement technology at Saarland University. His work focuses on the development of sensors and algorithms specifically with regard to bioinspired adhesive structures. He is particularly interested in inductive sensors and machine learning methods in order to develop simple but powerful sensors for complex tasks.

Sarah C.L. Fischer is currently Head of the Research Group MatBeyoNDT at Fraunhofer IZFP in Germany. After earning a Ph.D. in Materials Science in the area of bioinspired adhesive surfaces, she joined Apple's polymer engineering team in California to work on industrial applications of adhesives. After her stay in industry, she moved back to Germany to join Fraunhofer IZFP as a principal investigator and develop innovative experimental mechanics methods for complex materials at the interface of research and industry.

27511219, 2026, 7, Downloaded from https://advanced.onlinelibrary.wiley.com/doi/10.1002/adsr.70172 by Birgit Conrad-Markschläger - Fraunhofer IZFP , Wiley Online Library on [07/07/2026]. See the Terms and Conditions (https://onlinelibrary.wiley.com/terms-and-conditions) on Wiley Online Library for rules of use; OA articles are governed by the applicable Creative Commons License